HHS Public Access

Author manuscript

Cancer Res. Author manuscript; available in PMC 2016 April 01.

Published in final edited form as:

Cancer Res. 2015 April 1; 75(7): 1236–1243. doi:10.1158/0008-5472.CAN-14-3001.

In vivo tomographic imaging of deep seated cancer using fluorescence lifetime contrast

William L. Rice[1], **Daria M Shcherbakova**[2], **Vladislav V. Verkusha**[2,3], and **Anand T.N. Kumar**[1]

[1]Athinoula A. Martinos Center for Biomedical Imaging, Massachusetts General Hospital, and Harvard Medical School, Charlestown, Massachusetts 02129, USA [2]Department of Anatomy and Structural Biology, Albert Einstein College of Medicine, Bronx, New York 10461, USA [3]Department of Biochemistry and Developmental Biology, Institute of Biomedicine, University of Helsinki, Helsinki 00290, Finland

Abstract

Preclinical cancer research would benefit from non-invasive imaging methods that allow tracking and visualization of early stage metastasis in vivo. While fluorescent proteins revolutionized intravital microscopy, two major challenges which still remain are tissue autofluorescence and hemoglobin absorption, which act to limit intravital optical techniques to large or subcutaneous tumors. Here we employ time-domain technology for the effective separation of tissue autofluorescence from extrinsic fluorophores, based on their distinct fluorescence lifetimes. Additionally, we employ cancer cells labelled with near infra-red fluorescent proteins (iRFP) to allow deep-tissue imaging. Our results demonstrate that time-domain imaging allows the detection of metastasis in deep-seated organs of living mice with a more than 20-fold increase in sensitivity compared to conventional continuous wave techniques. Furthermore, the distinct fluorescence lifetimes of each iRFP enables lifetime multiplexing of three different tumors, each expressing unique iRFP labels in the same animal. Fluorescence tomographic reconstructions reveal 3D distributions of iRFP720-expressing cancer cells in lungs and brain of live mice, allowing ready longitudinal monitoring of cancer cell fate with greater sensitivity than otherwise currently possible.

Introduction

Fluorescent proteins (FPs) have revolutionized microscopic biological imaging as highly specific cell and gene expression markers (1). However, whole-body small animal imaging of FPs has still not been realized to its full potential. This is primarily due to high tissue absorption and autofluorescence (AF) in the visible wavelength regions where most current FPs of the GFP-like family absorb and emit light. Thus, deep tissue whole-body imaging using GFP-like FPs has required extremely large tumors and extended acquisition times (2–4). The near infrared (NIR) optical transparency window (~650–900 nm), where mammalian

Corresponding author: Anand T. N. Kumar, Room 2301, Athinoula Martinos Center, 149, 13th Street, Charlestown MA 02129, ankumar@nmr.mgh.harvard.edu, Phone: 617 726 6542.

Conflict of interest statement: The authors declare that they have no financial interest related to the work presented in this paper.

tissue absorption is minimized, is ideal for deep tissue whole-body imaging. Indeed, much effort in the past two decades has been focused on developing disease targeted NIR synthetic fluorophores for *in vivo* imaging (5,6). However, the task of identifying disease specific markers has proven to be challenging. As a result, much of the available targeted organic dyes exhibit significant non-specific uptake, reducing detection sensitivity (6–8). Recently, several types of genetically encoded NIR FPs, such as permanently fluorescent iRFPs (9), photoactivatable PAiRFPs (10) and iSplit reporter (11), that are excited and emit light in the NIR window have been developed and have shown great promise for whole-body optical imaging. A major challenge for the application of iRFPs to whole-body imaging of small and deep seated disease is their relatively low molecular brightness, which implies that tissue AF can still remain a significant contributor to the fluorescent signal. Although whole-animal imaging of iRFP-labeled tumors has been demonstrated (9,12,13), the tumors in these studies were either subcutaneous or consisted of several million cells in deep tissue. The ability to detect smaller metastases in deep organs of whole animals is of far more significance for pre-clinical oncology studies (14), since it will allow optimization of drug treatments to control the disease in its earliest stages. This motivates the development of techniques that can enhance the specificity for *in vivo* detection of iRFPs in the presence of background AF. More generally, the ability to image NIR FPs in deep tissue with high sensitivity will enable a wide range of applications ranging from detecting early stage disease to tracking gene expression (15).

Fluorescence lifetime contrast (16) using time domain (TD) detection (17–19) is a powerful mechanism for separating intrinsic tissue AF from extrinsic fluorescence. The lifetime characteristics of tissue AF are distinct from that of several FPs and NIR fluorophores. Furthermore, several fluorophores and FPs exhibit distinct *in vivo* lifetimes (20,18). Exploiting fluorescence lifetime contrast can thus allow two key advantages: (i) the rejection of tissue AF, thereby significantly enhancing imaging sensitivity, and (ii) the simultaneous detection of multiple targets in whole animals by labelling with fluorophores of distinct lifetimes (termed lifetime multiplexing). We have recently demonstrated the tomographic lifetime multiplexing of anatomically targeted fluorophores in living mice (20). We have also shown that fluorescence lifetime contrast allows for a greater than 25-fold increase in sensitivity over traditional continuous wave (CW) techniques for detecting subcutaneous tumors expressing GFP (21). Based on the NIR spectral properties of iRFPs and the dramatic increase in sensitivity afforded by fluorescence lifetime contrast, we investigated whether the pairing of these two technologies provides a viable option for deep tissue imaging in intact mice. Here we present the first demonstration of tomographic imaging of iRFPs in deep seated organs, such as the lungs and brain, using a fluorescence lifetime contrast.

Materials and Methods

Bacterial and mammalian cell culture

Bacterial LMG194 cells were transfected with pBAD-His/B plasmids (Life Technologies) encoding one of five iRFP proteins. Rat adenocarcinoma MTLn3 cells were obtained from Dr. John Condeelis (Albert Einstein College of Medicine, Bronx, NY). Cell line

authentication and validation was performed using immunofluorescence. MTLn3 cells stably expressing either iRFP670, iRFP702 or iRFP720 were obtained as previously described (9). Cells were maintained in α-MEM culture medium supplemented with 5% fetal bovine serum, 1% penicillin-streptomycin and 700 μg/ml G418 (all reagents from Life Technologies.)

Animal models

All procedures were performed in accordance with the Massachusetts General Hospital animal welfare guidelines. Female Nu/Nu mice were obtained from the Cox-7 defined-flora animal facility in MGH. Prior to experimentation, mice were either anesthetized or euthanized by inhaled isoflurane (2% or 5%, respectively).

To prepare cells for injection into animals, MTLn3-iRFP670, -iRFP702 and -iRFP720 cells were detached from culture dishes (TrypLE, Life Technologies), washed twice and re-suspended in calcium and magnesium free phosphate buffered saline (PBS, Life Technologies). For orthotopic injections, cells suspended in a 1:1 (v/v) PBS/matrigel (BD Biosciences) solution were injected in the mammary fat pad via 30 gauge needle. Tail vein injection of 2.5×10^4 to 2×10^6 cells in PBS were performed in a total volume of 150 μL. Intracranial injections were performed stereotactically in freshly sacrificed mice and consisted of 1×10^6 MTLn3-iRFP720 cells in 3 μL PBS at a rate of 300 nl/min. Cryopreservation was achieved by immersing sacrificed mice in liquid nitrogen followed by storage at −80°C. Slices of frozen mice were obtained using a cryotome blade and kept on dry ice until fluorescence imaging.

Imaging system

Time resolved images were acquired with a custom built imaging system described in detail previously (17). Briefly, fluorescence was excited by either the direct output of a titanium sapphire laser (Mai Tai, Spectra Physics; 800 nm at 80 MHz repetition rate,) tuned to 710 nm, or the pulsed broadband (500–850 nm) output of a Mai Tai driven photonic crystal fiber (Thorlabs NL-PM-750) filtered through a 650/40 nm filter. The resulting fluorescence emission was detected with either a 700 nm long pass filter, or a 750 nm longpass filter coupled to an intensified CCD camera (PicostarHR, LAVision; 12-bit cooled CCD, 300–500 ps gate width, 600 V gain, 150 ps steps, 4×4 hardware binning. The use of a CCD camera allowed a full field acquisition compared to fiber based detection. Excitation powers did not exceed ANSI standards for skin exposure to pulsed lasers. Camera integration times ranged from 0.3 to 3 s. Reflectance images (Figs. 1, 2h–j, 3d, 3f, 4f) were acquired by exposing the sample with the output of an optical fiber expanded with a diffusing filter (Thorlabs ED1-S50-MD). In the transmission measurements (Figs. 2b–g, 3, 4b, 4c), the output of the optical fiber was focused to a 1 mm diameter spot translated to multiple source locations below the mouse. The output power at each source was dynamically adjusted to ensure optimum usage of camera dynamic range (4096 counts). Full tomographic scans of the thorax (37 time gates, 28 sources) took 55 minutes while a 17 source scan of the mouse head was completed in less than 10 minutes. X-ray CT was obtained on a triple modality microPET-SPECT-CT imaging device (Triumph, GE Healthcare).

Image processing and tomographic reconstructions

Fluorescence image processing, X-ray CT segmentation, and fluorescence yield reconstruction algorithms were implemented in MATLAB (Mathworks, Natick). The full-field time domain data were processed in two different ways. First, fluorescence lifetime images were obtained by fitting the decay portion of time domain fluorescence measurements across the image with a single exponential function, $e^{-t/\tau(r)}$ where r denotes pixel location. The images of $\tau(r)$ constitute the lifetime maps shown in Figs. 1b, 1h, 2c and 2e. Secondly, decay amplitude images were obtained by fitting the decay portion of the time domain fluorescence measurements to the following dual-basis function:

$$U(t)=a_{AF}B(t)+a_{FP}e^{-t/\tau_{FP}}, \quad (1)$$

where *B(t)* is an empirically determined basis function representing tissue autofluorescence (obtained from naive animals and usually consisting of a biexponential decay), and a_{FP}, τ_{FP}, are the decay amplitude and lifetime of iRFP720 fluorescence. For both lifetime and decay amplitude analysis, pixels with intensities below 20% of the maximum intensity were rejected from the analysis. The recovered decay amplitudes of the AF (a_{AF}) and FP (a_{FP}) are assigned to the green and red components of a single RGB image matrix in Figs. 2f, 2g, 2j, 3d, 3f and 4c.

Tomographic reconstruction of the 3D distributions of iRFP fluorescence were performed using the asymptotic time domain (ATD) approach (22), which has been shown to be the optimal approach for tomographic lifetime multiplexing using the decay portion of the TD data (23). Briefly, the ATD approach directly relates the decay amplitude, a_{FP}, for the iRFP fluorescence (Eq. (1)) to the *in vivo* yield distribution, $\eta_{FP}(r)$, of iRFP fluorescence as the following linear forward problem:

$$a_{FP}(r_s, r_d)=\int d^3r W(r_s, r_d, r)\eta_{FP}(r), \quad (2)$$

where r_s, r_d are source and detector locations on the surface of the mouse, W is a reduced absorption CW sensitivity matrix for light propagation through tissue at the excitation and emission wavelengths (22), and r is the location of a voxel within the mouse. The weight function for the forward model, W, is a product of Greens functions at the excitation and emission wavelengths (24) and was computed using a GPU accelerated Monte Carlo algorithm (Monte Carlo Extreme, MCX (25)). Light propagation was simulated in a segmented mouse volume, derived from the X-ray CT images. The medium voxels corresponding to each CT-defined anatomical region were assigned tissue-specific optical properties (Supplemental Table 1).

The fluorescence yield distribution can be obtained by inverting Eq. (2), which is equivalent to the standard CW fluorescence tomography inversion (24). In order to improve the conditioning of the problem, the inversion was performed in two steps (26) . First, each CT-defined anatomical segment or region, such as lung, liver, bone, kidneys and heart, was assumed to have a constant value of iRFP fluorescence yield, η^j, where j denotes the index of the segment. This allowed a few parameter estimation of the fluorescence yield from the decay amplitudes using a reduced dimensional inversion problem, which was solved using a

fast fluorescence Monte Carlo algorithm based on stored photon path histories (27) . The η^j's recovered from the parameterized fit were next used to define a regularization matrix L of dimension (M X M) (where M is the number of medium voxels), whose diagonal elements are:

$$L=1/\sqrt{\eta^j}. \quad (3)$$

The matrix L was employed in a Tikhonov type inversion to recover the full fluorescence yield distribution $\eta(r)$ as follows (17):

$$\eta(r)=L^{-1}VS[S^2+\lambda I]U^T a_{FP}, \quad (4)$$

where U, S and V are obtained from a singular value decomposition of the weight matrix:

$$WL^{-1}=USV^T, \quad (5)$$

I is the identity matrix and λ is the regularization parameter. The singular value analysis of the weight matrix (Eq. 5) was implemented in MATLAB. The final reconstructed fluorescence yields were co-registered with X-ray CT in MATLAB and visualized in VolView 3.4 (Kitware Inc., Clifton Park, NY), as shown in Figs. 3a, 3c, 4d, and 4e.

Results and Discussion

In vitro lifetime imaging of iRFPs

First, we performed an initial screen of expression bacteria carrying five iRFP variants (9): iRFP670, 682, 702, 713, and 720 to determine their *in vitro* fluorescence lifetimes. Despite a 50 nm difference in the absorption maxima of iRFP670 and iRFP720, all variants display significant overlap in both their absorption and emission spectra (Figs. 1c,d). The spectral overlap allowed capture of TD reflectance fluorescence images from all five iRFPs simultaneously with a single excitation and emission filter set (650/40 nm and 700 nm long pass). As expected, the total CW fluorescence image, calculated as the area under the curve of the TD fluorescence signal (Fig. 1e), provides no contrast amongst the iRFPs (Fig. 1a). On the other hand, a single exponential fit of the TD fluorescence decay at each image pixel reveals the characteristic fluorescence lifetime of each iRFP (Fig. 1b). From this group of five iRFPs, there are three fully distinct and sharp fluorescence lifetime distributions (Fig. 1e,f) with mean (standard deviation) values of τ = 0.93 ns (σ = 0.02 ns), τ=0.78 ns (σ = 0.01 ns) and τ = 0.68 ns (σ = 0.008 ns). iRFP670 and iRFP682 share a similar fluorescence lifetime distribution (Fig. 1b; τ = 0.93 ns), as do iRFP713 and iRFP720 (Fig. 1b; τ = 0.68 ns).

In vivo lifetime multiplexing of three iRFPs in living mice

Next, to verify that the iRFP fluorescence lifetimes as measured in bacteria were maintained in mammalian cells, three iRFP variants were expressed in rat adenocarcinoma MTLn3 cells and grown in the mammary fat pad of mice. As for the *in vitro* case, tumors carrying iRFP670, iRFP702 or iRFP720 were indistinguishable in the CW reflectance fluorescence image (Fig. 1g) using a single excitation emission filter set, whereas fluorescence lifetime

(Fig. 1h) offered clear contrast between the iRFP expressing tumors. In these measurements, gut AF was minimized by feeding animals with alfalfa free diet. Gut AF can also be separated by taking advantage of the relatively long fluorescence lifetime (1.5 ns) compared to the iRFPs (Supplementary Fig. 1).

In vivo planar lifetime imaging of iRFP720 labelled cells in the live mouse lung

We next ascertained whether iRFPs can enable the detection of labeled cancer cells in the lungs of live mice. We introduced by tail vein injection, between 2.5×10^4 and 2.0×10^6 lung colonizing (28) MTLn3-iRFP720 cells into female nude mice, followed by transmission TD fluorescence measurements of the thorax. In order to ensure complete imaging coverage of the chest, multiple transmission TD fluorescence measurements were made with the excitation laser focused at different locations (source positions) under the mouse. These measurements were then combined into a single transmission TD fluorescence image. As seen in Figs. 2b,d, even in the NIR wavelengths (ex: 710 nm, em: 750 nm long pass), tissue AF was significant and dominated the CW fluorescence signal. Indeed, injection of 2.0×10^6 MTLn3-iRFP720 cells (Fig. 2d) resulted in only a 7% increase in CW fluorescence intensity. However, fluorescence lifetime images (Figs. 2c,e), generated by performing a single exponential fit to the decay portion of the TD fluorescence signal at each pixel on the mouse surface, reveal a significant increase in lifetime above the lungs (arrow Fig. 2e), post-injection of iRFP720 cells. Here, the measured lifetimes on the mouse surface above the lungs ($\tau \approx 0.5$ ns) do not match the iRFP720 lifetime (0.68 ns) observed from cells *in vitro*, since these values represent a mixture of the iRFP720 fluorescence and tissue AF. Furthermore, it is seen that minimal signal is detected in the central thoracic region (arrow Fig 2b) due to the strong absorption by the heart.

In order to confirm the localization of the MTLn3-iRFP720 cells *in vivo*, and to determine the true *in vivo* lifetime of iRFP720 fluorescence upon bio-distribution, we performed *ex vivo* reflectance TD fluorescence images on cryosections of sacrificed mice following tail vein injection. In cryosections through the thorax (Figs. 2h–j) it is clear that MTLn3-iRFP720 cells are confined to the lungs, and maintain a sharp fluorescence lifetime distribution with a mean lifetime of 0.68 ns *in vivo*, similar to the *in vitro* lifetimes. No significant fluorescence was detected in the other organs.

Knowledge of the *in vivo* lifetime of iRFP cells in the lungs, which equals the *in vitro* lifetime (as seen from Fig. 2j), allows the use of a dual basis function approach (18,21) to eliminate AF from the transmission TD fluorescence images. In this approach, the decay portion of the TD fluorescence was fit with a dual-basis function (Eq. 1 of Methods) consisting of a biexponential decay representing the tissue AF, determined experimentally before injecting cells, and a single exponential decay at the known *in vitro* fluorescence lifetime of iRFP720 ($\tau = 0.68$ ns). As a result, the contributions of iRFP720 fluorescence and tissue AF were separated into two independent fluorescence decay amplitude datasets, shown as red and green respectively in Figs. 2f,g,j. The dual basis function approach allows a dramatic increase in the contrast to background ratio (defined as the ratio of either the CW intensity or decay amplitude inside the lungs to that of the surrounding tissue (21)) of more than 20-fold by separating the iRFP720 fluorescence and tissue AF. Unlike the CW images

(Figs. 2b,d) the dual basis function approach clearly delineates the injected (Fig. 2g) from non-injected (Fig. 2f) mice, in which no iRFP720 fluorescence decay amplitude is recovered. Applying this technique, we were able to detect iRFP720 fluorescence down to approximately 5.0×10^4 MTLn3-iRFP720 cells dispersed in nude mouse lungs (Fig. 2l), surpassing the sensitivity of previous reports using CW fluorescence imaging in the lungs or other deep tissue organs (2,3,29,30). Separately, we also estimated the detection threshold for subcutaneously placed iRFP720 cells in live mice. As shown in Supplementary Figure 2, lifetime multiplexing enables the detection of approximately 1400 subcutaneous MTLn3-iRFP720 cells. This should be compared to the previously reported detection threshold of 5×10^4 subcutaneous iRFP cells using continuous wave fluorescence imaging (13).

Tomographic lifetime imaging of iRFP labelled cells in the live mouse lung

The fluorescence decay amplitudes corresponding to the iRFP720 lifetime, recovered from the basis function approach, as in Figs. 2g, can be directly used to recover the *in vivo* 3D distribution of MTLn3-iRFP720 cells using a previously established asymptotic TD (ATD) fluorescence lifetime tomography approach (22,27). X-ray CT scans, acquired after fluorescence imaging sessions, allowed for the segmentation of the mouse volume by tissue type, the assignment of tissue optical properties, and the use of anatomical priors in the fluorescence reconstruction algorithm (31). As seen in Figs. 3a,c, and Supplementary Video 1, the fluorescence yield reconstructions in mice that received cells i.v. indicate that the iRFP720 expressing cells are confined to the lung, and no non-specific fluorescence is reconstructed. The confinement of the fluorescence to the lungs is confirmed in cryosections of the thorax (Fig. 3d and Supplementary Fig. 3a–c), which closely match the tomographic fluorescence reconstructions overlaid on X-ray CT (Fig. 3c).

Longitudinal monitoring of MTLn3-iRFP720 fate in the mouse lung

To further demonstrate the advantage of the improved detection sensitivity of the ATD approach for monitoring cancer progression, we performed a longitudinal study of experimental metastasis production with 1×10^6 MTLn3-iRFP720 cells injected intravenously in nude mice (Fig. 3e,f). As observed in Figs. 3(a–d), the MTLn3 cells are rapidly dispersed throughout the lung following injection. The longitudinal progression of these emboli was followed by TD imaging and tomographic reconstructions using the ATD approach. Following injection, The ATD reconstructed iRFP720 fluorescence yield (Fig. 3e) showed a 10-fold increase in the injected mice compared to that observed from naive animals. Twenty four hours after injection, the fluorescence yield rapidly drops as the MTLn3-iRFP720 emboli are cleared by the mouse's innate immune system(32). Continued imaging illustrates the progress of experimental MTLn3-iRFP720 metastasis formation as those cells that were able to extravasate into the lungs continue to survive and grow. At 144 hours post injection, Mouse 3 exhibits the greatest recovered iRFP720 fluorescence yield in the tomography results, followed by Mouse 2 and Mouse 1. The relative iRFP720 fluorescence yields of Mouse 2 and Mouse 1 relative to Mouse 3 were, 0.36:1 and 0.22:1. These differences between the metastatic burden in the mice are confirmed in fluorescence amplitude images of cryosections from the corresponding mice (Fig 3f) in which the ratio of the total iRFP720 amplitude within four (2–3 mm thick) cryoslices were 0.37:1 (Mouse 2) and 0.10:1 (Mouse 1) relative to Mouse 3. Visually, bright, focal iRFP720 fluorescence was

observed in the cryosclices of Mouse 3, while fewer foci were visible in Mouse 2, and no bright iRFP720 foci were observed in Mouse 1 (Supplementary Fig 4). The cryosections in Fig. 3f showcase the significant autofluorescence (green) present in all the mice compared to the iRFP720 fluorescence (red) thus highlighting the sensitivity challenge posed to whole body imaging with CW imaging techniques alone. These results illustrate that the tomographic reconstructions using the ATD approach reflect the ground truth observed in the cryosections, establishing the great utility of TD imaging technology for longitudinal studies where an understanding of the total tumor/metastasis burden is necessary for both accurate tumor size matching of treatment groups and for real-time, animal specific, assessment of treatment outcomes (33).

Tomographic lifetime imaging of iRFP labelled cells in the mouse brain

Finally, we performed tomographic TD fluorescence imaging of the brain of sacrificed mice (Fig. 4). Point-like fluorescent inclusions, ~1 mm diameter and ~2.5 mm deep in the cerebrum were induced by stereotactic injection of 1×10^6 MTLn3-iRFP720 cells. As with imaging in the thorax (Fig 3), tissue AF is a significant contributor to the transmission CW images (Fig. 4b), with a 46% increase in CW fluorescence intensity observed following injection of MTLn3-iRFP720 cells. A dual basis function analysis of the TD fluorescence data (Fig. 4c) clearly delineates the iRFP720 fluorescence (red) from tissue AF (green). The ATD reconstruction of iRFP720 yield using the decay amplitudes of the 0.68 ns component indicate that the injected cells were limited to the left cerebral hemisphere (Fig 4d,e and Supplementary Video 2). This localization is confirmed in cryosections of the mouse head (Fig. 4f). The 3D localization error across multiple mice was 1.9 mm (0.6 mm S.D.) (n=5). This error is computed by comparing the location of the fluorescence yield reconstruction to an estimate of the true location of the injected cells derived from fluorescence images of mouse cryoslices (~3 mm thickness). This is necessary because the injections offer no X-ray contrast. These results demonstrate the advantage of the combination of iRFP720 cell labelling with fluorescence lifetime contrast for whole-body imaging of deep seated metastasis. It is noteworthy that studies in Figs. 3 and 4 are the first instance, to our knowledge, in which fluorescence optical tomography has been shown to detect cancer cell densities well below those visible in X-ray CT.

In summary, we have demonstrated the advantage of fluorescence lifetime contrast for whole-body imaging in the combination with the use of genetically encoded NIR FPs for highly specific labelling of cancer cells. Fluorescence lifetime contrast compliments the favorable spectral properties of iRFPs for deep tissue imaging by allowing the rejection of tissue AF, which has thus far remained a major impediment for whole-body fluorescence imaging. We have shown that lifetime contrast, using TD technology, enables *in vivo* imaging of iRFP720-expressing cancer cells in live mice, at levels well below current detection limits in deep tissues using continuous wave fluorescence methods. We have also demonstrated the ability to obtain three dimensional distributions of iRFP720 cancer cells in deep seated organs such as the lungs and the brain. The technique presented here should therefore allow precise localization of early stage metastasis across various organ systems and the efficient screening of cancer therapies (34). Moreover, we have shown that at least three of the iRFP variants exhibit distinct fluorescence lifetimes and can be separated in live

mice. We observe that to our knowledge, this is the first report of the lifetimes of iRFPs *in vitro* and in living mice. The ability to distinguish multiple iRFPs simultaneously present in a single animal using lifetime multiplexing hold great promise for visualizing multiple genetically encoded tags *in vivo.* More generally, the ability to detect NIR FPs in deep tissue with high sensitivity holds a promising future for translating existing applications of FPs from cell microscopy to whole-body imaging.

Supplementary Material

Refer to Web version on PubMed Central for supplementary material.

Acknowledgements

This work was supported by grants RO1-EB105325, CA164468, GM073913 and GM108579 from the US National Institutes of Health.

References

1. Chudakov DM, Matz MV, Lukyanov S, Lukyanov KA. Fluorescent Proteins and Their Applications in Imaging Living Cells and Tissues. 2010:1103–1163.
2. Hoffman RM, Yang M. Whole-body imaging with fluorescent proteins. Nat. Protoc. 2006; 1:1429–1438. [PubMed: 17406431]
3. Zacharakis G, Kambara H, Shih H, Ripoll J, Grimm J, Saeki Y, et al. ,Volumetric tomography of fluorescent proteins through small animals in vivo. Proc. Natl. Acad. Sci. U.S.A. 2005; 102:18252–18257. [PubMed: 16344470]
4. Yang M, Baranov E, Li XM, Wang JW, Jiang P, Li L, et al. Whole-body and intravital optical imaging of angiogenesis in orthotopically implanted tumors. Proc. Natl. Acad. Sci. U.S.A. 2001; 98:2616–2621. [PubMed: 11226288]
5. Bloch S, Lesage F, McIntosh L, Gandjbakhche A, Liang KX, Achilefu S. Whole-body fluorescence lifetime imaging of a tumor-targeted near-infrared molecular probe in mice. J. Biomed. Opt. 2005; 10:054003. [PubMed: 16292963]
6. Weissleder R, Tung CH, Mahmood U, Bogdanov A. In vivo imaging of tumors with protease-activated near-infrared fluorescent probes. Nat. Biotechnol. 1999; 17:375–378. [PubMed: 10207887]
7. Sosnovik DE, Nahrendorf M, Deliolanis N, Novikov M, Aikawa E, Josephson L, et al. Fluorescence tomography and magnetic resonance imaging of myocardial macrophage infiltration in infarcted myocardium in vivo. Circulation. 2007; 115:1384–1391. [PubMed: 17339546]
8. Goergen CJ, Chen HH, Bogdanov A, Sosnovik DE, Kumar ATN. In vivo fluorescence lifetime detection of an activatable probe in infarcted myocardium. J. Biomed. Opt. 2012; 17:056001. [PubMed: 22612124]
9. Shcherbakova DM, Verkhusha VV. Near-infrared fluorescent proteins for multicolor in vivo imaging. Nat. Methods. 2013:1–7. [PubMed: 23547284]
10. Piatkevich KD, Subach FV, Verkhusha VV. Far-red light photoactivatable near-infrared fluorescent proteins engineered from a bacterial phytochrome. Nat. Commun. 2013; 4:2153. [PubMed: 23842578]
11. Filonov GS, Verkhusha VV. A near-infrared BiFC reporter for in vivo imaging of protein-protein interactions. Chem. Biol. 2013; 20:1078–1086. [PubMed: 23891149]
12. Deliolanis NC, Ale A, Morscher S, Burton NC, Schaefer K, Radrich K, et al. Deep-Tissue Reporter-Gene Imaging with Fluorescence and Optoacoustic Tomography: A Performance Overview. Mol. Imaging Biol. 2014

13. Jiguet-Jiglaire C, Cayol M, Mathieu S, Jeanneau C, Bouvier-Labit C, Ouafik L, et al. Noninvasive near-infrared fluorescent protein-based imaging of tumor progression and metastases in deep organs and intraosseous tissues. J. Biomed. Opt. 2014; 19:16019. [PubMed: 24474505]
14. Talmadge JE, Singh RK, Fidler IJ, Raz A. Murine models to evaluate novel and conventional therapeutic strategies for cancer. Am. J. Pathol. 2007; 170:793–804. [PubMed: 17322365]
15. Marx V. Probes: seeing in the near infrared. Nat. Methods. 2014; 11:717–720. [PubMed: 24972170]
16. Lakowicz JR, Masters BR. Principles of Fluorescence Spectroscopy, Third Edition. J. Biomed. Opt. 2008; 13:029901.
17. Kumar ATN, Raymond SB, Dunn AK, Bacskai BJ, Boas Da. A time domain fluorescence tomography system for small animal imaging. IEEE Trans. Med. Imaging. 2008; 27:1152–1163. [PubMed: 18672432]
18. Kumar ATN, Chung E, Raymond SB, van de Water J, Shah K, Fukumura D, et al. Feasibility of in vivo imaging of fluorescent proteins using lifetime contrast. Opt. Lett. 2009; 34:2066–2068. [PubMed: 19572001]
19. Venugopal V, Chen J, Lesage F, Intes X. Full-field time-resolved fluorescence tomography of small animals. Opt. Lett. 2010; 35:3189–3191. [PubMed: 20890329]
20. Raymond SB, Boas DA, Bacskai BJ, Kumar ATN. Lifetime-based tomographic multiplexing. J. Biomed. Opt. 2010; 15:046011. [PubMed: 20799813]
21. Rice WL, Kumar ATN. Preclinical whole body time domain fluorescence lifetime multiplexing of fluorescent proteins. J. Biomed. Opt. 2014; 19:046005. [PubMed: 24715027]
22. Kumar AT, Raymond SB, Boverman G, Boas DA, Bacskai BJ. Time resolved fluorescence tomography of turbid media based on lifetime contrast. Opt. Express. 2006; 14:12255–12270. [PubMed: 19529654]
23. Hou SS, Rice WL, Bacskai BJ, Kumar ATN. Tomographic lifetime imaging using combined early- and late-arriving photons. Opt. Lett. 2014; 39:3–7.
24. Arridge SR, Schotland JC. Optical tomography: forward and inverse problems. Inverse Probl. 2009; 25:123010.
25. Fang Q, Boas DA. Monte Carlo simulation of photon migration in 3D turbid media accelerated by graphics processing units. Opt. Express. 2009; 17:20178–20190. [PubMed: 19997242]
26. Hyde D, Miller EL, Brooks DH, Ntziachristos V. Data specific spatially varying regularization for multimodal fluorescence molecular tomography. IEEE Trans. Med. Imaging. 2010; 29:365–374. [PubMed: 19758858]
27. Kumar ATN. Direct Monte Carlo computation of time-resolved fluorescence in heterogeneous turbid media. Opt. Lett. 2012; 37:4783–4785. [PubMed: 23164912]
28. Oku N, Sugawara M, Tsukada H, Irimura T, Okada S. Positron emission tomography analysis of metastatic tumor cell trafficking. Cancer Res. 1994; 54:2573–2576. [PubMed: 8168082]
29. Winnard PT, Kluth JB, Raman V. Noninvasive optical tracking of red fluorescent protein-expressing cancer cells in a model of metastatic breast cancer. Neoplasia. 2006; 8:796–806. [PubMed: 17032496]
30. Deliolanis NC, Kasmieh R, Wurdinger T, Tannous BA, Shah K, Ntziachristos V. Performance of the red-shifted fluorescent proteins in deep-tissue molecular imaging applications. J. Biomed. Opt. 2008; 13:044008. [PubMed: 19021336]
31. Radrich K, Ale A, Ermolayev V, Ntziachristos V. Improving limited-projection-angle fluorescence molecular tomography using a co-registered x-ray computed tomography scan. J. Biomed. Opt. 2012; 17:126011. [PubMed: 23208296]
32. Le Dévédec SE, van Roosmalen W, Maria N, Grimbergen M, Pont C, Lalai R, et al. An improved model to study tumor cell autonomous metastasis programs using MTLn3 cells and the Rag2(−/−) gammac (−/−) mouse. Clin. Exp. Metastasis. 2009; 26:673–684. [PubMed: 19466569]
33. Kodack DP, Chung E, Yamashita H, Incio J, Duyverman A, Song Y, et al. Combined targeting of HER2 and VEGFR2 for effective treatment of HER2-amplified breast cancer brain metastases. Proc. Natl. Acad. Sci. U.S.A. 2012; 109:E3119–E3127. [PubMed: 23071298]
34. Begley CG, Ellis LM. Drug development: Raise standards for preclinical cancer research. Nature. 2012; 483:531–533. [PubMed: 22460880]

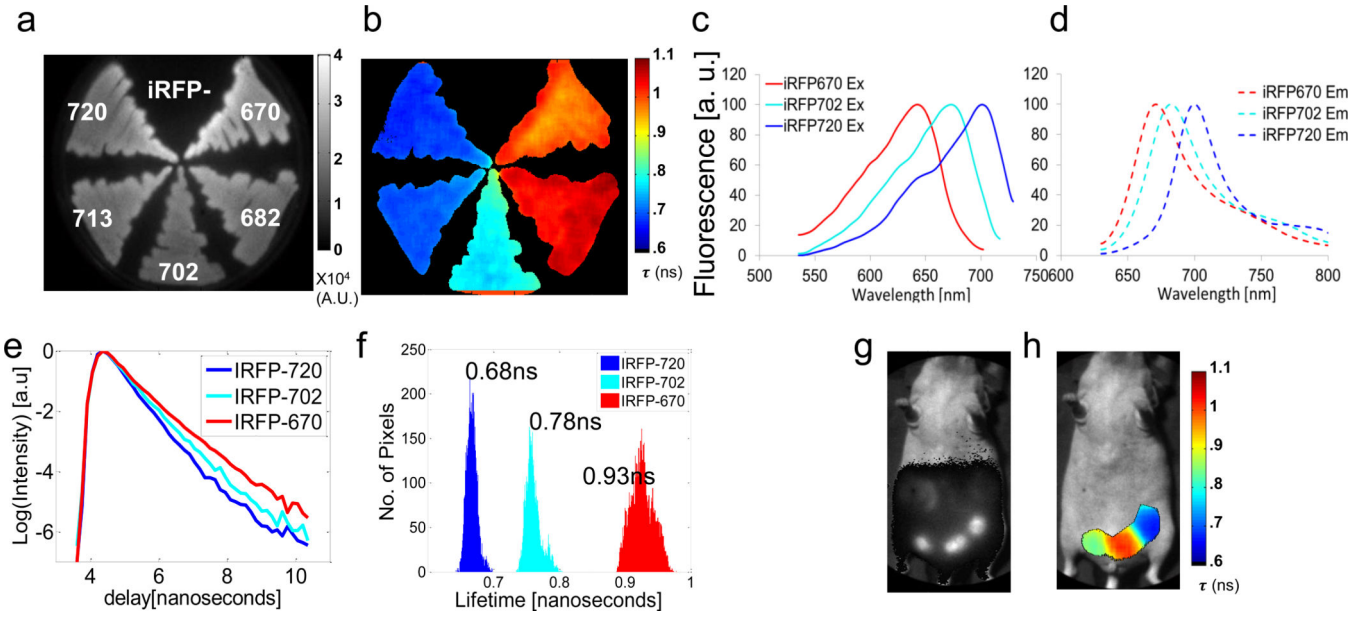

Figure 1. ***In vitro*** **and** ***in vivo*** **lifetime multiplexing of iRFPs**

All fluorescence data was acquired with single excitation/emission filter pair: ex: 650/40 nm, em: 700 nm long pass. (a) Continuous wave and (b) fluorescence lifetime images of bacteria expressing five iRFP variants (iRFP670, 682, 702, 713 and 720). (c) Normalized excitation and (d) emission spectra of iRFP670, 702 and 720. (e) TD fluorescence signal of iRFP670, 702 and 720 in bacteria. (f) Histogram of lifetime distribution derived from fluorescence lifetime image in (b). (g) Continuous wave and (h) fluorescence lifetime image of three MTLn3 tumors expressing iRFP670, 702 and 720 in the mammary fat pad of a female nude mouse.

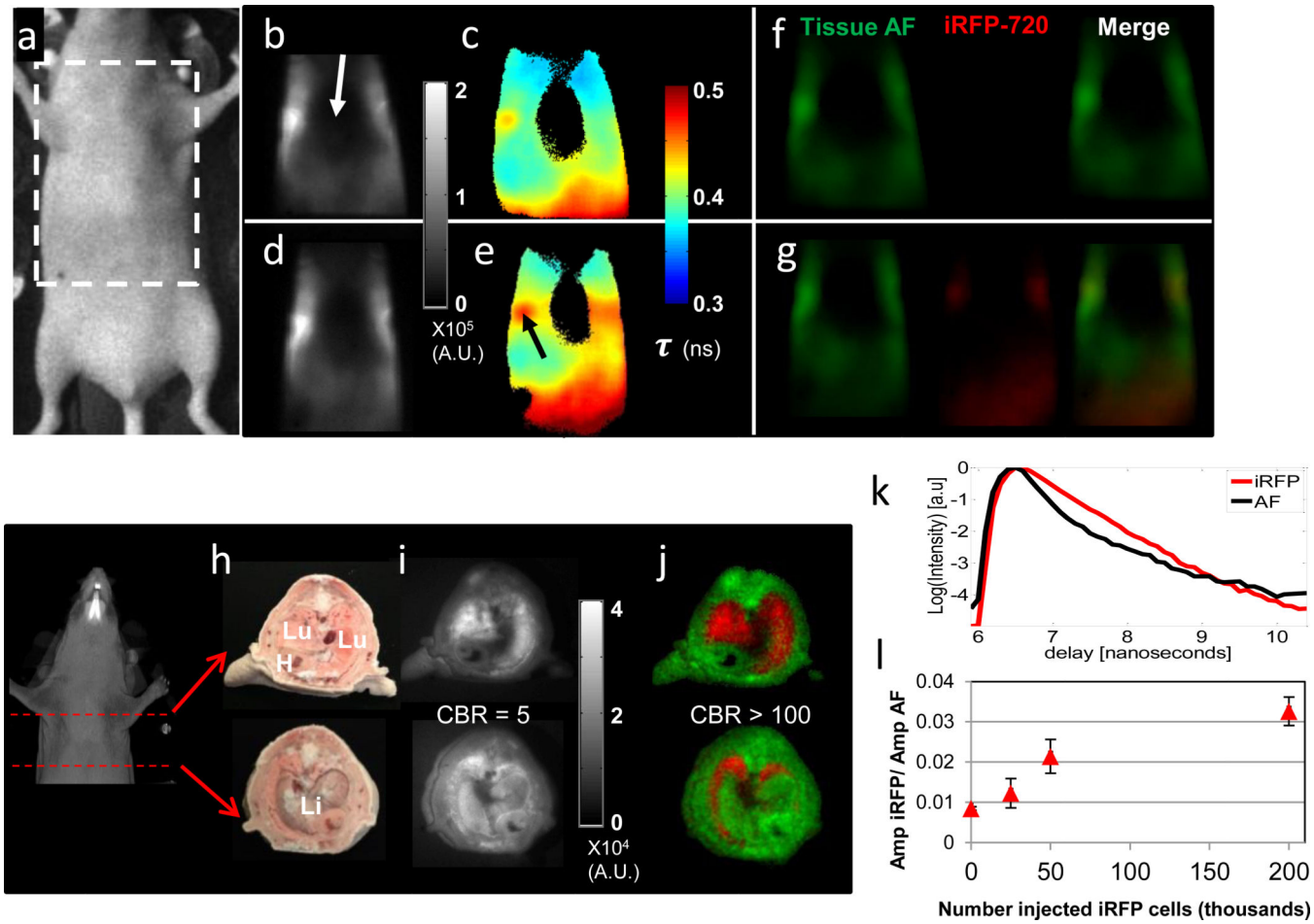

Figure 2. ***In vivo*** **and** ***ex vivo*** **planar lifetime imaging of iRFP720 labelled cells in the lungs**

(a) Snapshot and imaging region of interest. Transmission fluorescence images before (b, c, f) and after (d,e,g) i.v. injection of 2.0 ×10^6 MTLn3-iRFP720 cells. (b, d) CW fluorescence, (c, e) fluorescence lifetime images obtained from single exponential fits at each pixel and (f, g) fluorescence decay amplitudes of tissue AF (green) and iRFP720 (red) obtained from a dual basis function analysis (Eq. (1)) of transmission TD fluorescence measurements, shown separately and as a merged RGB image. (h) White light, Lu= lungs, Li=liver, H=heart, (i) CW fluorescence, and (j) Dual fluorescence decay amplitude images of cryosections from the thorax of a mouse following i.v. injection of 2.0×10^6 MTLn3-iRFP720 cells, showing AF (green) and iRFP720 (red) decay amplitudes as a single composite RGB image. (k) Representative TD fluorescence profiles of mouse tissue AF (black line) and iRFP720 (red line) from the cryosection measurements. (l) Ratio of iRFP720 to tissue AF fluorescence decay amplitude obtained from a dual basis function analysis of planar TD transmission fluorescence images of mice that received serial dilutions of MTLn3-iRFP720 cells via the tail vein.

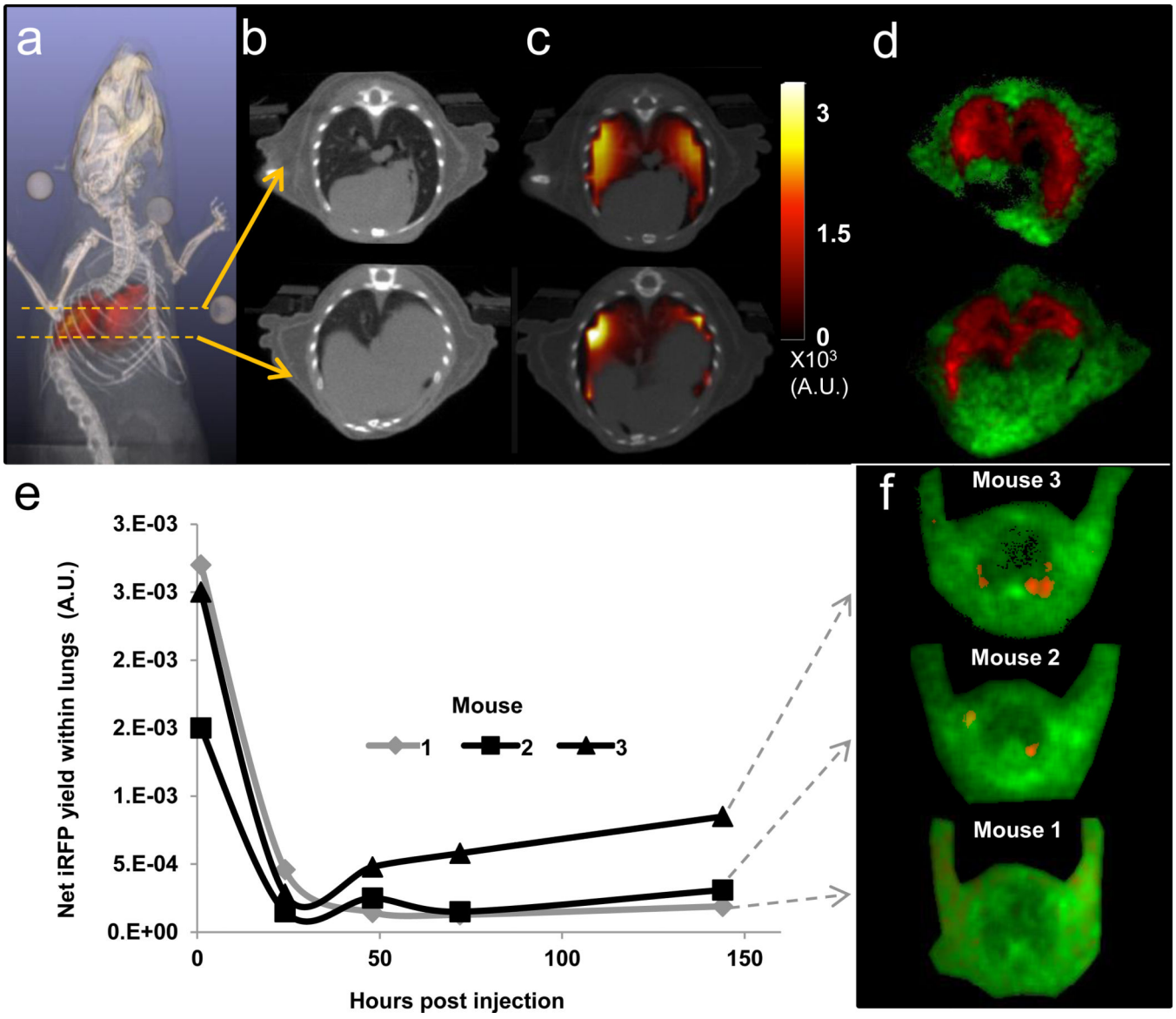

Figure 3. Tomography and longitudinal imaging iRFP720 cancer cells from the lungs

(a) Reconstructed *in vivo* fluorescence yield distribution (red) immediately following the injection of 2×10^6 MTLn3-iRFP720 cells in the tail vein of a nude mouse, co-registered with X-ray CT (grayscale) (See also Supplementary Video 1). Coronal slice of (b) the CT and (c) the ATD reconstruction of iRFP720 yield co-registered with CT. (d) Decay amplitude images obtained from dual basis function analysis (Eq. (1)) of reflectance TD images of lung cryosections of the same mouse shown in (a–c). AF (green) and iRFP720 (red) amplitudes are shown as a single RGB image. (e) Longitudinal study to monitor MTLn3 fate in three live nude mice following tail vein injection of 1×10^6 MTLn3-iRFP720 cells. Tomographic measurements were made from the injection time point up to 144 hours post injection. Net iRFP720 fluorescence yield within the lungs of the three mice, reconstructed using the ATD approach. (f) Decay amplitude images of lung cryoslices from

the three mice in (e) following sacrifice at 144 hours post injection, showing AF (green) and iRFP720 (red).

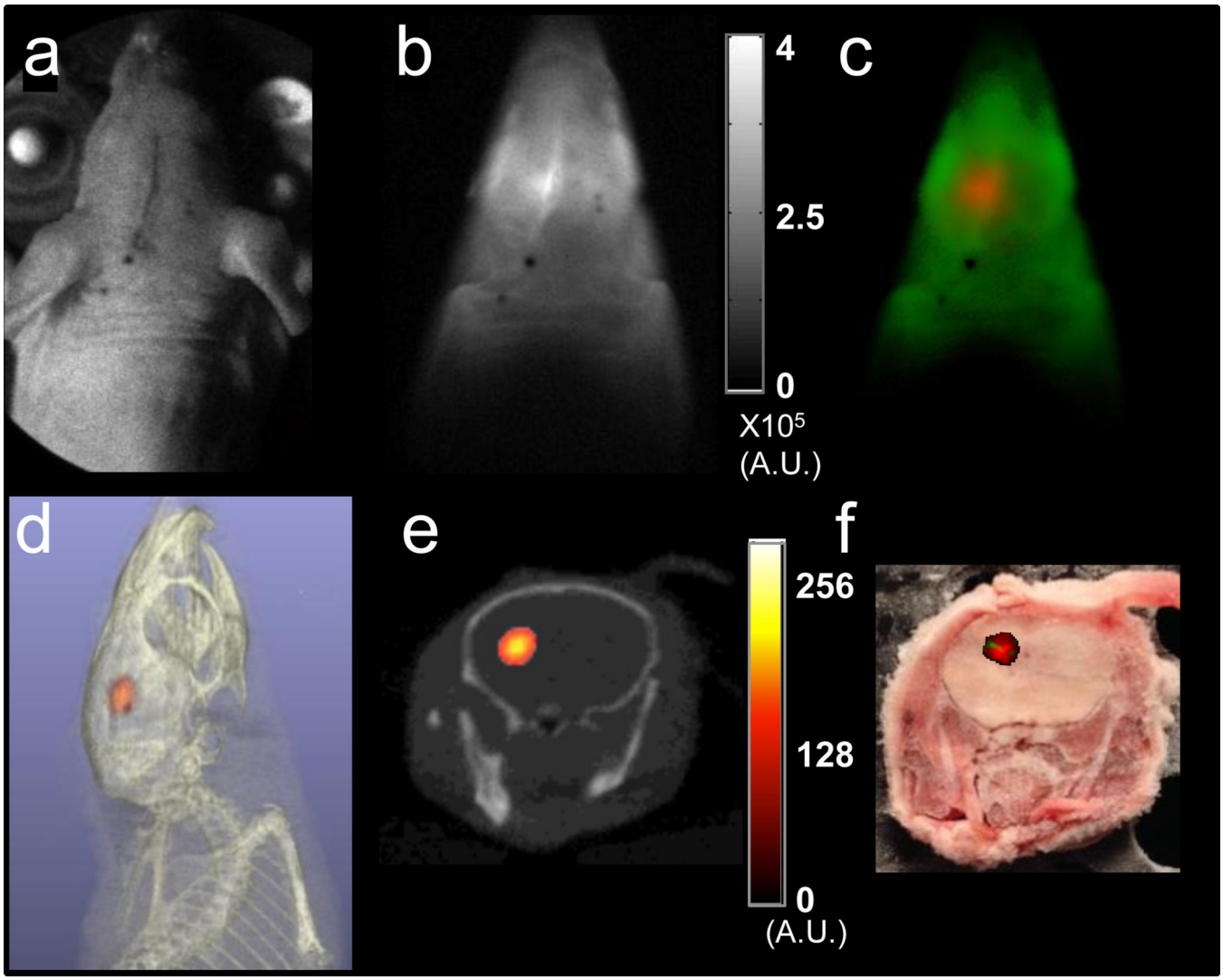

Figure 4. Tomography of iRFP720 tumors in the mouse brain

(a) White light image, (b) planar transmission CW fluorescence (integrated TD signal) and (c) fluorescence decay amplitude images for excitation source locations spanning the head of a sacrificed nude mouse following stereotactic injection of the left cerebral hemisphere with 1×10^6 MTLn3-iRFP720 cells in 3 μL. (c) shows the AF (green) and iRFP720 (red) decay amplitudes computed from the full TD data using a dual basis function approach (see Methods). (d) Volumetric and (e) coronal slice from tomographic reconstruction of iRFP720 fluorescence yield distribution (red) in the mouse head coregistered with X-ray CT (grayscale). (f) Snapshot of cryosection slice corresponding to the anatomical location depicted in (e) with co-registered overlay (red) of iRFP fluorescence decay amplitude showing the location of the tumor.